RF microplasmas with energies suited to *in situ* selective cleaning of surface adsorbates in ion microtraps

Mariam Akhtar[1,2], Guido Wilpers[1], Kaushal Choonee[1], Erling Riis[2] and Alastair G. Sinclair[1]

[1] National Physical Laboratory, Teddington, TW11 0LW, UK
[2] University of Strathclyde, Glasgow, G4 0NG, UK

E-mail: `alastair.sinclair@npl.co.uk`

Abstract.

We have demonstrated a capacitively-coupled, RF microplasma inside the 3D electrode structure of an ion microtrap device. For this work, devices with an inter-electrode distance of 340 μm were used. The microplasmas were operated at $\Omega_{RF}/2\pi$ = 23 MHz, in both He and He:N_2 gas mixtures, over a range of RF amplitudes (140 V to 220 V) and pressures (250 mbar to 910 mbar). Spectroscopic analysis of the He I 667 nm and Hα 656 nm emission lines yielded the gas temperature and electron density, which enabled calculation of the mean ion bombardment energy. For the range of operating parameters studied, we calculated mean He$^+$ energies to be between 0.3 eV and 4.1 eV. While these energies are less than the threshold for He sputtering of hydrocarbon adsorbates on Au, we calculate that the high energy tail of the distribution should remove adsorbate monolayers in as little as 1 minute of processing. We also calculate that the distribution is insufficiently energetic to have any significant effect on the Au electrode surface within that duration. Our results suggest that the microplasma technique is suited to *in situ* selective removal of surface adsorbates from ion microtrap electrodes.

1. Introduction

Trapped atomic ions are an important physical system for investigating quantum information processing [1], quantum simulation [2], quantum metrology [3], and optical atomic clocks [4]. The ability to store and cool ions, virtually isolated from the surrounding environment, has been essential for taking advantage of their quantum behaviour [5]. In the aforementioned applications, several sources of decoherence can hinder high-fidelity coherent control of the ions' quantum state; one of the foremost is motional decoherence [6–9]. Minimising this to negligible levels in microfabricated ion traps is paramount for development of quantum technologies based on trapped ions. Motional decoherence is due to fluctuating electric fields [6, 8, 10], however the exact origin of this electric field noise is still not well understood.

Ions in microfabricated traps [7], where the ion-electrode distance (d) is typically in the range 80 μm $\leqslant$ d $\leqslant$ 250 μm, are particularly sensitive to this noise, which has been found to scale as $\sim 1/d^4$ [6, 8, 11, 12]. Moreover, resultant heating rates are routinely well above that which would be expected from Johnson noise, giving rise to the term "anomalous heating" [8]. For example at $d \leqslant 365$ μm, ion heating rates in room-temperature traps have been shown to be more than three orders of magnitude above the value expected from Johnson noise [8, 13]. Cooling of trap electrodes with liquid N_2 to 150 K [9], and with liquid He to 6 K [14], was observed to reduce room-temperature heating rates by 1 and 7 orders of magnitude respectively. However even at low temperatures the motional heating rate is still notably above the level due to Johnson noise alone. For example, in [14, 15] the measured heating rates at cryogenic temperatures were still 3 orders of magnitude greater than the value expected from Johnson noise.

Models have shown that the observed scaling of heating rates with distance can be explained by fluctuating patch potentials [6, 8] or by thin dielectric layers (*i.e.* native oxide or hydrocarbons) on electrodes [10]. The latest experimental results [12, 16] support the latter model. It is noted that a clean Au surface exposed to air would acquire 0.4 monolayers of hydrocarbon coverage within a few minutes, and that a vacuum-bake procedure can increase coverage to a few monolayers [10]. In addition, ion microtraps of planar electrode geometry have been used to investigate the influence of electrode surface composition on trapped ion heating rate. A correlation was observed between the removal of carbon adsorbed on electrode surfaces, and a hundred-fold reduction of the heating rate [17, 18]. A further investigation concerned noise due to carbon adatom diffusion on Au surfaces [19], which showed a model for electric field noise in line with measurements.

We have developed monolithic ion microtrap devices which are in the form of a linear, segmented trapping array [20–22]. These devices have a 3D electrode structure which maximises the depth and harmonicity of the trapping potential. However, this 3D structure also makes it inappropriate for treatment of Au electrode surfaces by the ion beam method discussed above. In addition to removing contaminants, an energetic beam (*e.g.* with Ar$^+$ energies of 300 - 2000 eV [17, 18]) will also remove Au electrode material since the sputtering threshold for Au with Ar$^+$ is 15 eV [23]. Redeposition of Au on dielectric surfaces, intended as insulating gaps in the electrode structure, risks the creation of an electrical short thus failing the device.

In contrast, a gentler approach to surface processing has been investigated previously by introducing a coil near the surface of the trap to generate an Ar inductively-coupled plasma [24]. The ion bombardment energies produced were approximately 20 eV, which should be compared to 30 eV threshold for sputtering the Nb electrodes of the trap in question. Therefore, the process is more likely to be selective in the sputtering of only hydrocarbon material from the electrode surface. Using this method, a four-fold reduction in heating rate was reported. We adopt an alternative approach which avoids the need for an inductive coil in the system. Instead, we generate a capacitively-coupled, RF microplasma by using the ion trap electrodes themselves. We show this to be suited to *in situ*, low-energy, selective sputtering of only the hydrocarbon contaminants on electrode surfaces, and not the Au of the electrodes themselves. This could be a useful technique in future studies of electric field noise, for separating the effects of surface cleanliness from any due to electrode surface order [25].

This paper presents measurements to assess the suitability of using a microplasma for selective sputtering of adsorbed hydrocarbon contaminants from electrode surfaces in an ion microtrap device. In order to do this, the mean ion bombardment energy (ϵ_{bom}) and particle fluxes need to be determined. The quantity ϵ_{bom} depends on two essential parameters of the microplasma, namely the gas temperature (T) and the electron density (n_e). We used optical emission spectroscopy (OES) to obtain both of these plasma parameters. Due to the small length scales of a microplasma, diagnosing the parameters can be very difficult without perturbing the plasma. OES is an established, non-intrusive method which is well-suited to measuring these parameters, despite the small length scales involved [26, 27]. On determining these plasma parameters, ϵ_{bom} was calculated using a model

that incorporates high-voltage collisional sheaths with a capacitively-coupled, radio-frequency (RF) discharge [28]. Furthermore, particle fluxes incident on the electrode surface were determined, permitting surface cleaning times to be estimated.

Section 2.1 describes the apparatus used to obtain the spectroscopic measurements from a microplasma in the ion microtrap device. Central to the method presented is that T and n_e are determined from measured spectral linewidths. Section 2.2 details several different broadening mechanisms which need to be accounted for. The methods used to determine the parameters T and n_e are described in section 2.3. Section 3 describes the method for calculating ϵ_{bom} and surface adsorbate removal times. Data from both pure and mixed-gas microplasmas is presented in section 4. The use of the technique for surface treatment of ion microtrap electrodes is considered in section 5.

2. Experiment and method

2.1. Experimental setup

This work used ion microtrap devices of a monolithic, 3D electrode geometry, similar to that described in our earlier publication [20]. The devices are made by metallisation and micromachining of a 350 μm-thick SiO_2-on-Si wafer [21]; the Au electrode pattern is laid down on the SiO_2. Figure 1a illustrates the cross-sectional format and material system of the electrode microstructure. Figure 1b shows an example chip packaged in a ceramic leadless chip carrier. For this investigation, two architectures of microtrap were used. The first is a linear array of three trapping zones (figure 1c) [20], whereas the second has seven trapping zones and a spatially separated ion loading zone (figure 1d); hereafter these are referred to as type A and type B microtraps respectively.

A microtrap device was cleaned with a low-power, oxygen microwave plasma asher for 2 minutes, after which it was exposed to atmosphere for up to 1 day. Following this, it was contained under vacuum in a stainless steel chamber, similar to the form of that detailed in [22], where the ceramic carrier forms the electrical feedthrough for the vacuum (see figure 2). This procedure is almost identical to that used to package a device for ion trapping experiments. Hydrocarbon surface adsorbates accumulate on the Au electrodes during exposure to air (and also during vacuum bakeout when preparing a device for ion trapping) [10]. In contrast to [22], butyl rubber under pressure forms the vacuum seal between the stainless steel and ceramic chip carrier. This sealing method is sufficient for pumping down to pressures $P = 10^{-7}$ mbar yet it permits rapid and straightforward swapping of devices under test. The vacuum pumping and gas lines are so configured as to permit pumping of the chamber, as well as the introduction of gas and gas mixtures at controlled partial pressures.

A capacitively-coupled RF microplasma is created in the 340 μm-wide microtrap aperture by applying a voltage (of amplitude 130 V $\leqslant U_{RF} \leqslant$ 230 V and frequency $\Omega_{RF}/2\pi = 23$ MHz) to the RF electrodes of the device (see figure 1a). The RF signal source is a National Instruments PXI 5404 with variable attenuator (Minicircuits ZX73-2500-S+) for amplitude control. This signal is amplified (Minicircuits ZHL-5W-1) and drives a tank circuit which includes the microtrap. A bi-directional coupler (Minicircuits ZFBDC20-61HP+) between the amplifier and the tank circuit samples the forward and reflected powers which, with the measured build-up factor of the tank circuit, are used to calculate U_{RF} on the electrodes. The microplasma could be achieved with He and a He:N_2 gas mixture where both gases were from sources of 99.999 % purity. Testing with N_2 alone was also possible, but this required U_{RF} beyond the range of the specific test chips used in this study. To generate the microplasma, the DC electrodes of the device (see figure 1a) were grounded and the compensation electrodes were unconnected. It was observed that by leaving the Si bulk ($\rho = 2.6 \times 10^{-3}$ Ωcm) electrically floating, a more homogeneous and stable microplasma was produced in the aperture.

The apparatus used to record the optical emission spectrum from the microplasma is illustrated in figure 2; this is similar to others reported [26, 29–31]. A pair of achromatic lenses image the microplasma emission into a multi-mode fibre. The lenses and fibre are fixed with respect to each other, however this assembly can be translated in three dimensions which affords some spatial resolution. Another achromatic lens couples the imaged light from the fibre into to an imaging spectrometer (Horiba iHR550). The spectrum is detected by an electron-multiplying CCD camera (Andor Newton DU971N-FI), and the extent of the microplasma generated is monitored by a CMOS camera (Thorlabs DCC3240M).

At the operating parameters studied, microplasma emission was relatively weak. To record a spectral lineshape with sufficient signal-to-noise at a specific set of microplasma operating parameters, 10 sequential EMCCD exposures, each of 10 s duration, were averaged. Sequential acquisitions permitted the detection of any time-varying microplasma instability. Without a microplasma operating, the mean background spectrum was recorded using the same detection parameters. The lineshape with background subtracted was used for analysis and determination of the plasma parameters.
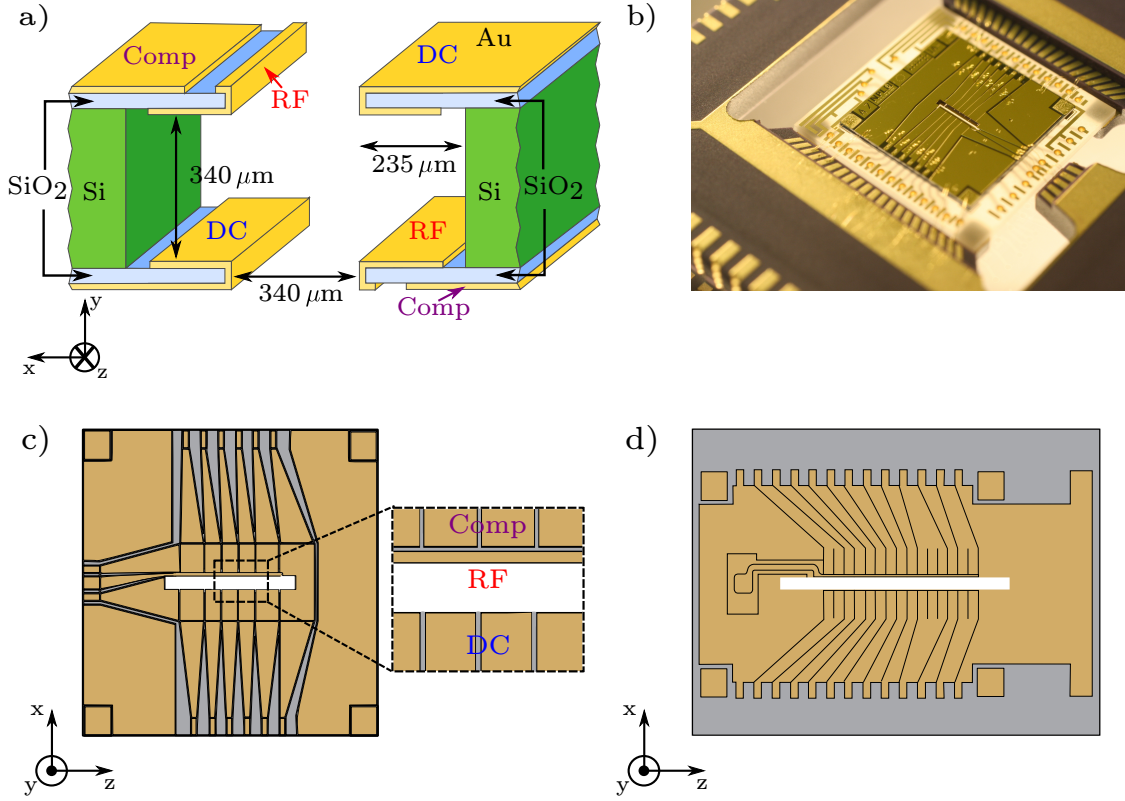
Figure 1. a) Schematic diagram showing the cross-sectional format of the trap chip aperture. This single-segment cut-out shows the material system of the ion microtrap. These features are identical for both type A and type B traps. Note that electrodes are on both front and back sides of the 3D micro-structure. b) Example of a type A microtrap in an electronic package. c) Front-side electrode layout of microtrap type A. The magnified inset shows the detail of the RF and DC electrodes around the trap aperture. Rotating the chip around the trap axis (z) by 180° would result in the same image from the back-side electrode layout. Chip dimensions are 8.4 mm × 8.4 mm with a 2.6 mm long aperture. d) Front-side electrode layout of microtrap type B; as in c), the back-side layout is identical. Chip dimensions are 11.0 mm × 8.4 mm with a 6.4 mm long aperture.

2.2. Optical diagnostics

To determine the gas temperature (T) and the electron density (n_e), the linewidths of two spectral features emitted by the microplasma were analysed; specifically these were the He I 667 nm line and the Hα 656 nm Balmer Line [32]. In some microplasmas (where $n_e \leqslant 10^{12}$ cm^{-3}), the Stark broadening of the He I 667 nm line is negligible [33]. However, in the experiments reported here (10^{14} cm$^{-3} \leqslant n_e \leqslant 10^{15}$ cm^{-3}), the Stark broadening of the He I 667 nm line must be taken into account [34]. Therefore, both measured spectral lines depend on T and n_e. The Hα 656 nm line is particularly sensitive to n_e and is well documented in the literature [35, 36]. Despite no deliberate introduction of H into the system, the Hα line was evident and was attributed to dissociation of trace water vapour [37, 38] in the vacuum.

The spectral spread of optical emission from the microplasma consists of Lorentzian and Gaussian components which convolve to yield a Voigt profile. The linewidth of the Gaussian component, $\Delta\lambda_G$, is defined as

$$\Delta\lambda_G = (\Delta\lambda_I^2 + \Delta\lambda_D^2)^{1/2} \qquad (1)$$

where $\Delta\lambda_I$ and $\Delta\lambda_D$ are the contributions arising from instrument and Doppler broadening respectively. The spectrometer property $\Delta\lambda_I$, verified to be of Gaussian form, was measured using He-Ne laser radiation prior to each data run. A fit (using a Levenberg-Marqardt algorithm) to the resultant spectral lineshape gave values in the range 0.029(4) nm. The linewidth of the Lorentzian component, $\Delta\lambda_L$, is a combination of van der Waals, resonance and Stark broadening, which are quantified by linewidth contributions $\Delta\lambda_{VW}$, $\Delta\lambda_R$ and $\Delta\lambda_S$ respectively:

$$\Delta\lambda_L = \Delta\lambda_{VW} + \Delta\lambda_R + \Delta\lambda_S . \qquad (2)$$

In the analysis that follows, equations quoted from the literature often contain particular quantities in non-SI
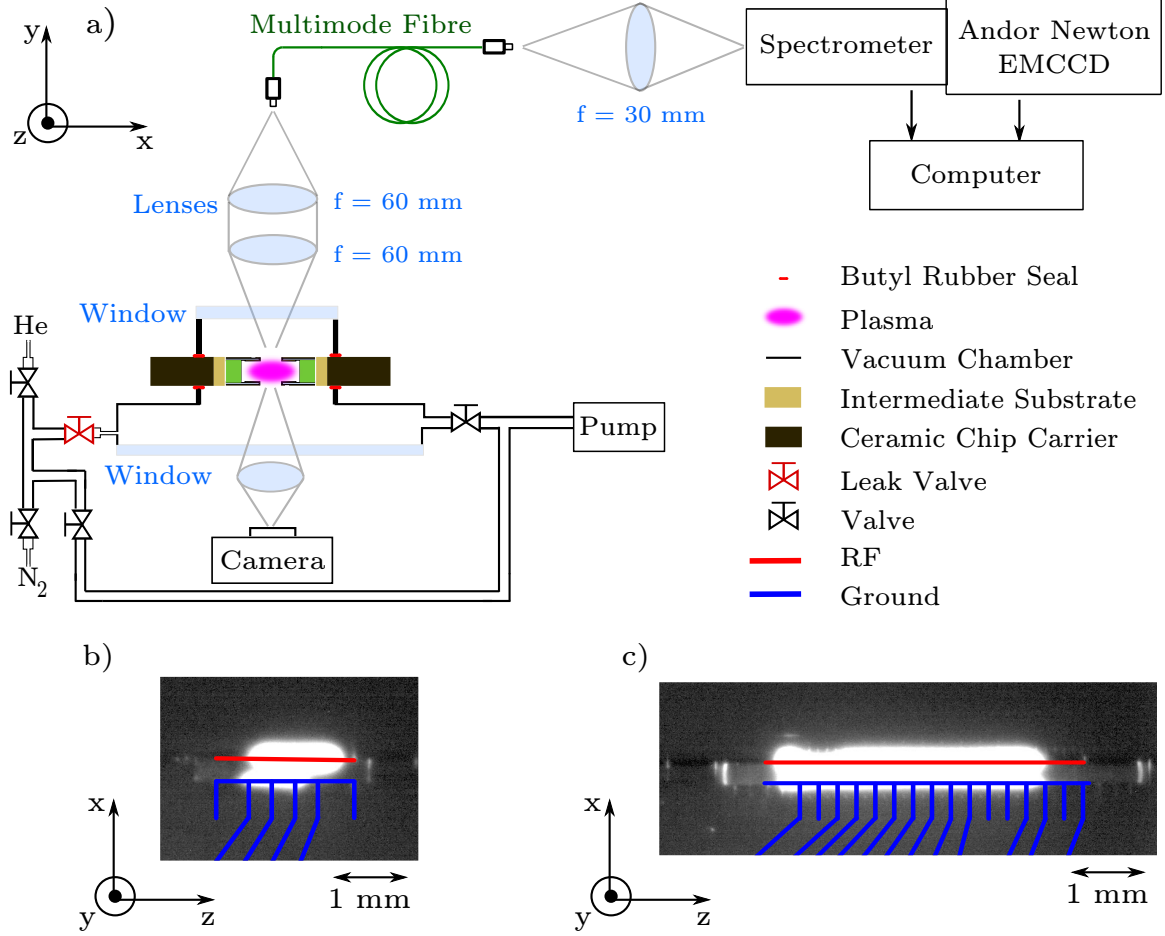
Figure 2. a) Experimental setup for optical emission spectroscopy. A pressure gauge (not shown) measures the vacuum and gas pressures in the chamber. The light emitted by the microplasma is imaged using a lens pair (with unit magnification) into a multimode fibre (50 μm core diameter, 0.22 NA). From the fibre, light is imaged (with magnification of 0.7) into a 0.55 m imaging spectrometer, where the detector array is an electron-multiplying CCD (pixel size of 16 μm). The spectrometer entrance slit width was set to 34 μm, and a 1200 lines/mm grating was used to achieve a measured resolution of 0.029(4) nm. Images of the microplasma were recorded by a CMOS camera at normal incidence to the trap aperture. b) Example of trap type A generating a He microplasma at $P = 390$ mbar, $\Omega_{RF}/2\pi = 23$ MHz and $U_{RF} = 154$ V. c) Example of trap type B generating a He microplasma at $P = 400$ mbar, $\Omega_{RF}/2\pi = 23$ MHz and $U_{RF} = 160$ V. The electrode boundaries are overlaid on the images in b) and c). Exposure time was 93 ms for both images.

units for ease of use. In this section, wavelengths and linewidths are in units of nm. Other parameters with non-SI units are specified; otherwise SI units apply.

2.2.1. Doppler broadening
The velocity distribution of ions and atoms in the microplasma leads to a range of Doppler shifts associated with any spectral line. The resultant Doppler broadening contribution to the linewidth, $\Delta\lambda_D$, is well documented [26, 34, 39, 40], and can be written as

$$\Delta\lambda_D = 2.918 \times 10^{-20}\lambda_0\left(\frac{T}{M}\right)^{1/2} \tag{3}$$

where λ_0 is the centre transition wavelength, T is the temperature of the emitters and M is atomic mass of the emitter. Here T is assumed to be equal to the gas temperature in the microplasma due to the high collisional frequency between the emitters and neutral atoms.

2.2.2. Resonance broadening
Resonance (or self) broadening [41] occurs due to collisions with neighbouring identical species, where the transition giving rise to the spectral emission has an upper or lower energy level with an electric dipole coupling to the ground state [39]. The associated contribution to linewidth, $\Delta\lambda_R$, can be calculated using [32, 34, 41]

$$\Delta\lambda_R = 8.61 \times 10^{-28} \left(\frac{g_L}{g_U} \right)^{1/2} \lambda_r f_r \lambda_0^2 n_{emit} \quad (4)$$

where $g_{L(U)}$ is the statistical weight of the lower (upper) level of the transition, λ_r and f_r are respectively the resonance wavelength and the oscillator strength of the transition coupling to the ground state, and n_{emit} is the density of emitter atoms in the ground state (in cm^{-3}).

2.2.3. Van der Waals broadening

Van der Waals broadening results from the dipole of the excited emitter particle interacting with the induced dipole of the surrounding ground state atoms during a collisional process. The equations and relationships to quantify this broadening mechanism are detailed in [39] and reproduced here. The associated contribution to spectral linewidth, $\Delta\lambda_{VW}$, is given by

$$\Delta\lambda_{VW} = 8.18 \times 10^{-19} \lambda_0^2 (R^2 \alpha)^{2/5} \left(\frac{T}{\mu} \right)^{3/10} n_g \quad (5)$$

where R^2 is a transition-dependent constant (in units of the Bohr radius a_0), α is the average polarisability (in cm^3), μ is the emitter-perturber reduced mass (in amu) and n_g is the neutral gas density (in cm^{-3}). Here R^2 can be calculated as $R^2 = R_U^2 - R_L^2$, where L(U) is the lower (upper) energy level of the transition,

$$R_{L(U)}^2 = \frac{n_{L(U)}^{*2}}{2} (5n_{L(U)}^{*2} + 1 - 3l_{L(U)}(l_{L(U)} + 1)). \quad (6)$$

The orbital quantum number of the transition level is denoted by $l_{L(U)}$ and the square of the effective quantum number $n_{L(U)}^{*2}$ is

$$n_{L(U)}^{*2} = \frac{I_H}{I_{IP} - E_{L(U)}} \quad (7)$$

where I_H is the ionisation potential of hydrogen, I_{IP} is the ionisation potential of the emitter atoms (both in cm^{-1}) and $E_{L(U)}$ is the energy of the lower or upper levels of interest (in cm^{-1}). The average polarisability of the emitter can be estimated using

$$\alpha = \frac{9}{2} a_0^3 \left(\frac{3I_H}{4E_{ex}} \right)^2 \quad (8)$$

where the Bohr radius a_0 is in units of cm, E_{ex} (in cm^{-1}) is the energy of the first excited level of the perturber particles.

2.2.4. Stark broadening

Due to the presence of charged perturbers in the microplasma such as ions and electrons, the Stark effect can broaden the spectral emission. The magnitude of the effect varies across different species. The Stark broadening contribution to the linewidth, $\Delta\lambda_S$, for H lines in an non-equilibrium discharge (as in this work), can be written as [42]

$$\Delta\lambda_{S,H} = 2.05 \times 10^{-11} n_e^{0.63} \quad (9)$$

where n_e is in cm^{-3}. For He I lines, the analysis in [43] permits the Stark broadening of these lines to be calculated as

$$\Delta\lambda_{S,He} = 2\omega_0 \left(\frac{n_e}{n_{e,0}} \right) \left[1 + 1.75\alpha_0 \left(\frac{n_e}{n_{e,0}} \right)^{1/4} \times \right.$$
$$\left. \left(1 - 0.068n_e^{1/6} T_e^{-1/2} \right) \right], \quad (10)$$

where the electron impact half-width $2\omega_0$ (in nm) and the ion broadening parameter α_0 can be found for a range of values of the reference electron density $n_{e,0}$ (in cm^{-3}) and T_e [43, 44].

2.3. Lineshape fitting procedure

This section describes how the plasma parameters T, n_e (which are necessary for calculating ϵ_{bom}) were determined from spectral emission at a specific combination of P and U_{RF}. A particular problem with fitting a Voigt function to a spectral feature is that the Gaussian and Lorentzian components can vary over a wide range, yet produce very similar lineshapes [26]. For example, the Hα 656 nm lineshape is a function of T and n_e, but due to the low signal-to-noise ratio of this emission, multiple solutions are possible. Therefore a two-line Voigt function was fitted (using a Levenberg-Marquardt algorithm) to a spectrum consisting of the Hα 656 nm and the He I 667 nm lines; the linewidths are dependent on T and n_e, which were free parameters in the fit.

The function fitted to the two-line spectrum was

$$f_{V,H,He} = f_{V,H} + f_{V,He} \quad (11)$$

where the Voigt lineshape $f_{V,x}$ ($x \in \{H, He\}$) is given by [26]

$$f_{V,x} = \frac{2ln2\Delta\lambda_{L,x}}{\pi^{3/2}\Delta\lambda_{G,x}^2} \times$$
$$\int_{-\infty}^{+\infty} \frac{\exp(-t^2)}{\left(2(ln2)^{1/2} \frac{(\lambda-\lambda_0)}{\Delta\lambda_{G,x}} - t \right)^2 + \left((ln2)^{1/2} \frac{\Delta\lambda_{L,x}}{\Delta\lambda_{G,x}} \right)^2} dt. \quad (12)$$

The lineshapes $f_{V,H}$ and $f_{V,He}$ have components $\Delta\lambda_L$ and $\Delta\lambda_G$ appropriate for the Hα and He I spectral lines. The constants associated with fitting a Voigt lineshape to these spectral features are listed in table 1.

Table 1. Constants, defined in the text, which are used in the fitting procedure outlined in section 2.3. He and Hα denote the He I 667 nm and Hα 656 nm transitions respectively. In lines 9 - 12, the subscripts a and b denote values corresponding to an electron temperature $T_e = 20000$ K and 40000 K (1.72 eV and 3.45 eV) respectively, which covers the range in the experiments reported here. These ω_0 and α_0 are referenced at $n_{e,0} = 10^{18}$ cm^{-3}.

Transition	Symbol	Value	Reference
He	g_L	1	[41]
He	g_U	3	[41]
He	λ_r	58.4334 nm	[41]
He	f_r	0.2762	[41]
He	I_{IP}	198311 cm^{-1}	[41]
He	E_L	171135 cm^{-1}	[41]
He	E_U	186105 cm^{-1}	[41]
He	E_{ex}	171135 cm^{-1}	[41]
He	ω_{0a}	3.66 nm	[44]
He	ω_{0b}	3.29 nm	[44]
He	α_{0a}	0.52	[44]
He	α_{0b}	0.56	[44]
He, Hα	I_H	109737 cm^{-1}	[39]
Hα	E_L	82259 cm^{-1}	[45]
Hα	E_U	97492 cm^{-1}	[45]

Since the Hα emission arises from a trace gas, $\Delta\lambda_R$ was neglected in that instance. Using the relations shown in equations (1) - (3), (5) and (9), $\Delta\lambda_{G,H}$ and $\Delta\lambda_{L,H}$ are described by

$$\Delta\lambda_{G,H} = (\Delta\lambda_I^2 + 5.129 \times 10^{-13}\lambda_0^2 T)^{1/2} \qquad (13)$$

and

$$\Delta\lambda_{L,H} = \left(4.652 \times 10^{-11}\frac{P\lambda_0^2}{T^{7/10}}\right) + (2.05 \times 10^{-11}n_e^{0.63}), \qquad (14)$$

where n_e is in cm^{-3}.

The He I 667 nm line depends on $\Delta\lambda_I$, $\Delta\lambda_D$, $\Delta\lambda_R$, $\Delta\lambda_{VW}$ and $\Delta\lambda_S$. From equations (3), (4), (5) and (10) the He line is also a function of T and n_e. The Voigt function in equation (12) can then be re-written with $\Delta\lambda_{G,He}$ and $\Delta\lambda_{L,He}$ in the form

$$\Delta\lambda_{G,He} = (\Delta\lambda_I^2 + 1.282 \times 10^{-13}\lambda_0^2 T)^{1/2} \qquad (15)$$

and

$$\Delta\lambda_{L,He} =$$
$$\left(3.537 \times 10^{-11}\frac{P\lambda_0^2}{T^{7/10}}\right) + \left(5.811 \times 10^{-10}\frac{P_{emit}\lambda_0^2}{T}\right) +$$
$$\frac{2\omega_0 n_e}{10^{18}}\left(1 + \alpha_0 n_e^{1/4}1.75 \times 10^{-4.5}\left(1 - 0.068n_e^{1/6}T_e^{-1/2}\right)\right), \qquad (16)$$

where P_{emit} is the partial pressure of the emitters and n_e is in cm^{-3}. The Stark broadening parameters ω_0 and α_0 are referenced at $n_{e,0} = 10^{18}$ cm^{-3} and the values used in this work can be found in table 1. A linear interpolation between documented values was used in order to determine the parameters for a given T_e. Equation (16) depends on T_e, which in turn is a function of T. The method used to calculate T_e for a given T can be found in Appendix A.1. Since T_e cannot be solved analytically, then for each iteration of the fitting routine, a new value for T_e is calculated numerically (using a Newton-Raphson method). An example of a fit used to determine n_e and T is shown in figure 3. For ease of comparison to other published data, n_e and T can be applied to the relevant equations in section 2.2 to calculate broadening contributions $\Delta\lambda_D$, $\Delta\lambda_{VW}$, $\Delta\lambda_S$ and $\Delta\lambda_R$.

3. Quantifying surface effects

Once T and n_e have been measured, three plasma parameters must be calculated, to enable subsequent calculation of the principal parameters of interest. Appendix A describes the detail of how the electron temperature $T_e(T)$, the ion velocity $u_s(T,n_e)$ and density $n_s(T,n_e)$ at the sheath edge were calculated. From these three parameters, the average surface bombardment energies for ions can be calculated using models set out in [28] and [46]. Additionally, the flux of particles with sufficient energy to sputter surface adsorbates can be determined; in turn, this can be used to estimate times required to clean the microtrap electrode surfaces from adsorbates. The discharge studied in this work is a low-frequency, capacitively-coupled discharge at high pressure and with high-voltage, collisional sheaths. This specific regime permits some standard approximations in the calculations. In the equations presented in this section, all quantities are in SI units. However, specific values for energies are quoted in eV to be consistent with the literature on this topic.

3.1. Calculating the ion bombardment energy

In a collisional microplasma, the maximum sheath thickness s_m is greater than the mean free path λ_i of an ion [28]. As an ion is accelerated across the sheath, the
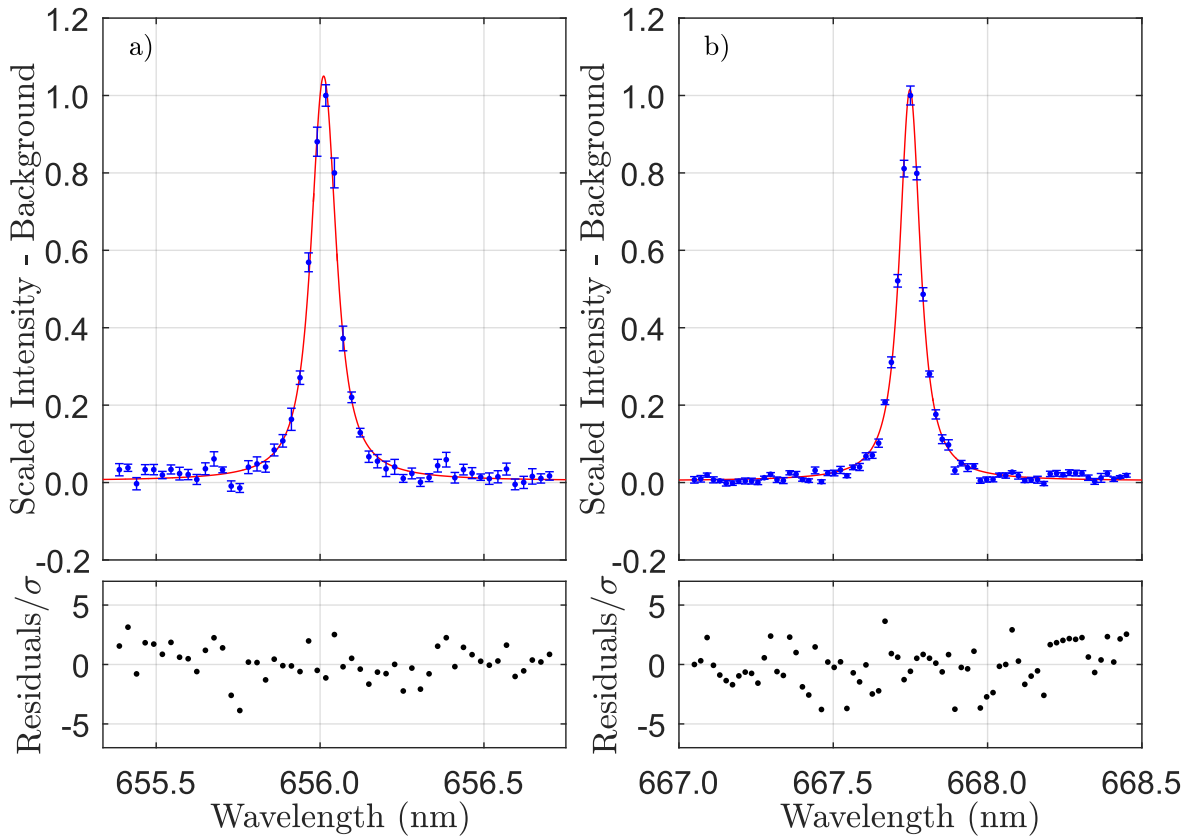
Figure 3. Examples of He I 667 nm and Hα 656 nm spectral line data observed at plasma parameters of $P = 590$ mbar, $\Omega_{RF}/2\pi = 23$ MHz and $U_{RF} = 182$ V. From the fit to both lineshapes (see equations (11) - (16)), $T = 323(12)$ K and $n_e = 5.8(7)\times10^{14}$ cm^{-3}, where the errors are 1σ statistical from the fit only. a) Hα 656 nm line data (blue points) and Voigt lineshape fitted using equations (12), (13) and (14). Broadening contributions: $\Delta\lambda_I$=0.0261 nm, $\Delta\lambda_D$= 0.0085 nm, $\Delta\lambda_{VW}$=0.0207 nm, $\Delta\lambda_S$=0.0408 nm. The studentised residuals are shown below the lineshape. b) He I 667 nm line data (blue points) and Voigt lineshape (red line) fitted using equations (12), (15) and (16). Broadening contributions: $\Delta\lambda_I$=0.0261 nm, $\Delta\lambda_D$= 0.0043 nm, $\Delta\lambda_{VW}$=0.0183 nm, $\Delta\lambda_R$=0.0473 nm, $\Delta\lambda_S$=0.0046 nm. The studentised residuals are shown below the lineshape.

resulting collisions dissipate energy and lead to lower surface bombardment energies. Here λ_i is calculated using the hard sphere model via [28]

$$\lambda_i = \frac{k_B T}{\sigma P} \qquad (17)$$

where k_B is the Boltzmann constant and σ is the collisional cross-section for the particular particle interaction in question [28]. For a He-He collision $\sigma_{He-He} = 1.36\times10^{-19}$ m^2 [46]. For a He$^+$-He interaction we calculate the mean of the energy-dependent cross-section in the 1-10 eV range to be $\sigma_{He^+-He} = 3.10\times10^{-19}$ m^2 [28, 47].

The typical mean free path of an ion is in the sub-micron range. In addition, the time-varying sheath thickness is given by [28]

$$s(t) = \left[1.43\epsilon_0 \left(\frac{2e\lambda_i}{\pi M}\right)^{1/2} \frac{V_s(t)^{3/2}}{en_s u_s}\right]^{2/5} \qquad (18)$$

where e is the electronic charge, M is the ion mass, ϵ_0 is the free-space permittivity, and $V_s(t)$ is the time-varying sheath voltage.

Since the discharge is of low-frequency character, *i.e.* the RF drive frequency is much less than the ion plasma oscillation frequency, the ions respond to the instantaneous electric field. Furthermore, the electron energy relaxation time ($\sim$ 3 ps) is shorter than the RF period (43 ns) and as a result, the electron energy distribution is strongly modulated by the applied RF field. Therefore, the sheath can be approximated as a succession of DC sheaths at different points in the RF phase [27]. The sheath voltage V_s for a low-frequency plasma with high-voltage sheaths, *i.e.* where $eV_s \gg k_B T_e$, is [28]

$$V_s = \begin{cases} U_{RF} \sin(\Omega_{RF} t), & 2n\pi < \Omega_{RF} t < (2n+1)\pi, \\ 0, & (2n-1)\pi \leqslant \Omega_{RF} t \leqslant 2n\pi. \end{cases} \qquad (19)$$

For the plasma regime in this work, the ion

bombardment energy, and the flux energy distributions of the ions and neutrals discussed in section 3.2, can be found following the analysis of Hagelaar *et. al.* [46]. The time-varying mean ion bombardment energy γ is given by

$$\gamma = \frac{eE}{n_g \sigma_{He^+ - He}}. \tag{20}$$

Here, n_g is the gas density, $\sigma_{He^+ - He}$ refers to collisions in the sheath and the electric field E in the sheath is [28]

$$E = \left(\frac{3en_s u_s}{2\epsilon_0 (2e\lambda_i / \pi M)^{1/2}} \right)^{2/3} s^{2/3}, \tag{21}$$

where s has a time dependence according to equation (18). The time-averaged mean bombardment energy $\epsilon_{bom} = \frac{1}{t} \int_0^t \gamma dt$ is calculated using equations (18), (20) and (21). The sheath voltage is effective at accelerating the ions to the electrode over only half of the RF cycle (equation (19)), thus

$$\epsilon_{bom} = \frac{eE_0}{\pi n_g \sigma} \int_0^\pi (\sin \theta)^{2/5} d\theta, \tag{22}$$

where $\theta = \Omega_{RF} t$ and E_0 is the electric field when $V_s = U_{RF}$.

3.2. Estimating the adsorbate removal time

As ions are accelerated in the sheath, collisions result in a flux of both neutral atoms (with time-varying energy distribution $\Gamma_n(\epsilon)d\epsilon$) and ions (with time-varying energy distribution $\Gamma_i(\epsilon)d\epsilon$) impacting upon the electrode surface. Approximate surface processing times can be calculated for both the ions and neutral atoms; this relies on knowing the time-averaged particle flux incident on the electrode surface, Φ_x where $x \in \{i, n\}$.

Noting the current continuity condition [28] and subsequently that $\int_0^\infty \Gamma_i(\epsilon)d\epsilon = n_s u_s$, then at an instantaneous value of sheath voltage, the time-varying energy distribution of the ion flux at the surface is

$$\Gamma_i(\epsilon)d\epsilon = \frac{n_s u_s}{\gamma} \exp \left(-\frac{\epsilon}{\gamma} \right) d\epsilon. \tag{23}$$

To calculate Φ_i in an oscillating low-frequency sheath, the instantaneous ion flux must also be time-averaged over half of the RF cycle. After accounting for the 50 % duty cycle of the sputtering process, Φ_i is given by

$$\Phi_i = \frac{1}{2\pi} \int_{\epsilon_{th}}^{\epsilon_{up}} \int_0^\pi \frac{n_s u_s}{\gamma_0 (\sin \theta)^{2/5}} \times \\ \exp \left(\frac{-\epsilon}{\gamma_0 (\sin \theta)^{2/5}} \right) d\theta d\epsilon. \tag{24}$$

Here, γ_0 is the instantaneous mean ion bombardment energy when $E = E_0$, and $\epsilon_{th} = 12.3$ eV is the sputtering threshold (see section 4). ϵ_{up} is the absolute upper limit of the ion energy (*i.e.* no collisions when crossing the sheath at maximum potential), which is given by

$$\epsilon_{up} = \frac{M}{2} \left(\frac{2s_m e E_0}{M} + u_s^2 \right). \tag{25}$$

Typically, 330 eV $\leqslant \epsilon_{up} \leqslant$ 500 eV.

The bounds of the neutral flux energy distribution $\Gamma_n(\epsilon)d\epsilon$ for an instantaneous sheath voltage are given in [46]. The upper and lower limits respectively are given by

$$\Gamma_n(\epsilon)d\epsilon < \frac{\sigma_{He^+ - He}}{\sigma_{He - He}} \left(1 + \frac{2\gamma}{\epsilon} + \frac{2\gamma^2}{\epsilon^2} \right) \Gamma_i(\epsilon)d\epsilon \tag{26}$$

and

$$\Gamma_n(\epsilon)d\epsilon > \frac{\sigma_{He^+ - He}}{\sigma_{He - He}} \Gamma_i(\epsilon)d\epsilon. \tag{27}$$

Φ_n is calculated in a similar fashion to Φ_i as above, at both limits of $\Gamma_n(\epsilon)d\epsilon$. From these two limits, a mean value of Φ_n is calculated. In doing so, this requires calculation of $\sigma_{He^+ - He}$ [28, 47] in the range $\epsilon_{th} \leqslant \epsilon \leqslant \epsilon_{up}$; we use a mean value (weighted with respect to $\Gamma_n(\epsilon)d\epsilon$) of $\sigma_{He^+ - He} = 2.1 \times 10^{-19}$ m^2.

The removal of an adsorbed hydrocarbon layer is described by the rate equation [48]

$$\frac{dN_a}{dt} = -\Phi_x \sigma_a N_a(t), \tag{28}$$

where N_a is the adsorbate surface density and σ_a is the sputtering cross-section calculated following the approach of [48, 49]. Note that a limitation of this approach is that it does not take into account redeposition of the sputtered material through processes such as back-diffusion and back-scattering [50, 51].

Solving equation (28) gives $N_a = N_0 \exp(-t/\tau_a)$, where N_0 is the initial adsorbate surface density and $\tau_a = (\Phi_x \sigma_a)^{-1}$ is the time constant for the process. The time taken to reach a target surface density for the adsorbate, N_t, is then given by

$$t_{clean} = \left(\ln \frac{N_0}{N_t} \right) \tau_a. \tag{29}$$

An estimate of $N_a(t = 0) = N_0$ for a hydrocarbon adsorbate was made on the basis that the average H-C bond length is 110 pm [52]; assuming a grid of these bonds in two monolayers, we estimate $N_0 = 4.1 \times 10^{19}$ m^{-2}. In reality, the hydrocarbon density will depend on the exact structure of the hydrocarbons themselves and the adsorption sites that exist on the electrode surface.

4. Results and discussion

In the remainder of this paper we quote values for energies, electron density and pressure in eV, cm^{-3} and mbar for consistency with the literature on this topic.

It is advantageous to maximise the microplasma coverage of electrodes, to minimise redeposition of sputtered particles [51] onto trapping electrode surfaces. Figures 2b,c present two example images to illustrate the coverage that was attained. Quantitative data on the electrode coverage for a single trap chip of each type is presented in figure 4. This shows that adequate coverage of the trapping zones can be achieved for trap type B at 330 mbar $\leqslant P \leqslant$ 440 mbar. In trap type A the microplasma covers both sides of the aperture less symmetrically than in type B, resulting in incomplete trapping zone coverage. However at data points corresponding to $P = \{390, 450, 490\}$ mbar coverage is almost complete. Improved coverage would result from a higher U_{RF}, but this was not possible due to limitations of the particular test device used here.

Four microtrap chips, two of each device type, were used to make repeated spectroscopic measurements in a pure He microplasma. Figure 5a shows the voltage amplitudes U_{RF} at which the plasma spectroscopic measurements were recorded. These amplitudes do not correspond to the threshold for plasma breakdown, but instead to the conditions where the microplasma had the greatest coverage and homogeneity over the extent of the device aperture. The spectroscopy measurements were recorded over a pressure range of 350 - 910 mbar for trap type A and a range of 290 - 490 mbar for trap type B. Two primary factors limited the ranges of U_{RF} and pressure. First, the microplasma can become delocalised; we observed light emitted outside the aperture and along the tracks on the surface of the device. Secondly, there was also the risk of generating a microplasma at the wirebonds that make the electrical connection from the ceramic chip carrier to the trap. In both cases, a plasma constriction could sputter the electroplated Au and result in electrical shorts. With the normal microplasma operating conditions established, the plasma was confined to the microtrap aperture when struck.

The gas temperature T and electron density n_e were determined using the methods in section 2 and the results can be seen in figure 5b,c. For a microplasma maximally distributed in the trap aperture, T shows a positive correlation with pressure, ranging from around room temperature up to as much as $\sim$ 460 K. This is to be expected from pressure alone, however note that for some data sets, the increase in U_{RF} accompanying the pressure increase (see figure 5a) is also expected to raise T [33,40,42,53]. Typical values of T for microplasmas under similar conditions have been reported in the range 300 K $\lesssim T \lesssim$ 600 K [32,33,54]. A low gas temperature in the microplasma is beneficial since it decreases the possibility of thermal damage to the microtrap. The error bars in figure 5 comprise uncertainties due to the statistics of the fit (1σ), the Stark and instrument broadening components, and in some instances a small but noticeable deviation from the ideal Voigt lineshape.

It has been pointed out in other work [55] that semiclassical theory calculations of neutral atom Stark-broadened linewidths agree with experiment to within $\pm$ 20 %. From analysis of the fitting routine, we estimate that this contributes additional uncertainties of only $\pm$ 2 % to T and $\pm$ 1 % to n_e. We estimate that the uncertainty in the instrument broadening contributes uncertainties of $\pm$ 1 % in T and $\pm$ 2 % in n_e. For a few data points, the results of the fitting routine appear to suggest values of T below room temperature. However, in those instances we observe that the wings of the He I lineshape deviate by a small amount from the ideal Voigt profile (the cause of this is not known). In such cases, the fit overestimates the Lorentzian component and thus underestimates T. From further analysis, we estimate that the associated systematic errors in T and n_e are + 45 K and + 4×10^{13} cm^{-3} for those particular points. In those cases, these errors are added to the upper error bounds of both quantities. For those points, T then extends above room temperature.

Micro-scale plasmas operate at a much higher pressure than those on a larger scale. As a result, they can also obtain higher densities of charged particles. The results for the measured n_e are presented in figure 5c. A weighted, linear, least-squares fit to the measured n_e showed a weak positive correlation with increasing pressure and voltage over the ranges tested. This observed trend is consistent with literature [53, 56].

Using the data in figures 5b,c, the time-averaged mean bombardment energies ϵ_{bom} were calculated and are displayed in figure 5d. The results show that within the voltage and pressure ranges tested, the mean ion bombardment energy is 0.3 eV $\leqslant \epsilon_{bom} \leqslant$ 2.1 eV (this is the range covered by the data and associated error bar extremes). These results are consistent with ϵ_{bom} calculated using numerical simulations of He microplasmas operating in a regime similar to that reported here. For example, simulations of microplasmas in a device with a 200 μm electrode spacing, operating at 200 V $\leqslant U_{RF} \leqslant$ 400 V, $\Omega_{RF}/2\pi =$ 13.56 MHz and $P = 1000$ mbar, have shown mean bombardment energies that ranged from 1 eV $\leqslant \epsilon_{bom} \leqslant$ 3 eV [27].

During the proposed microplasma processing procedure, it is essential that while contaminants
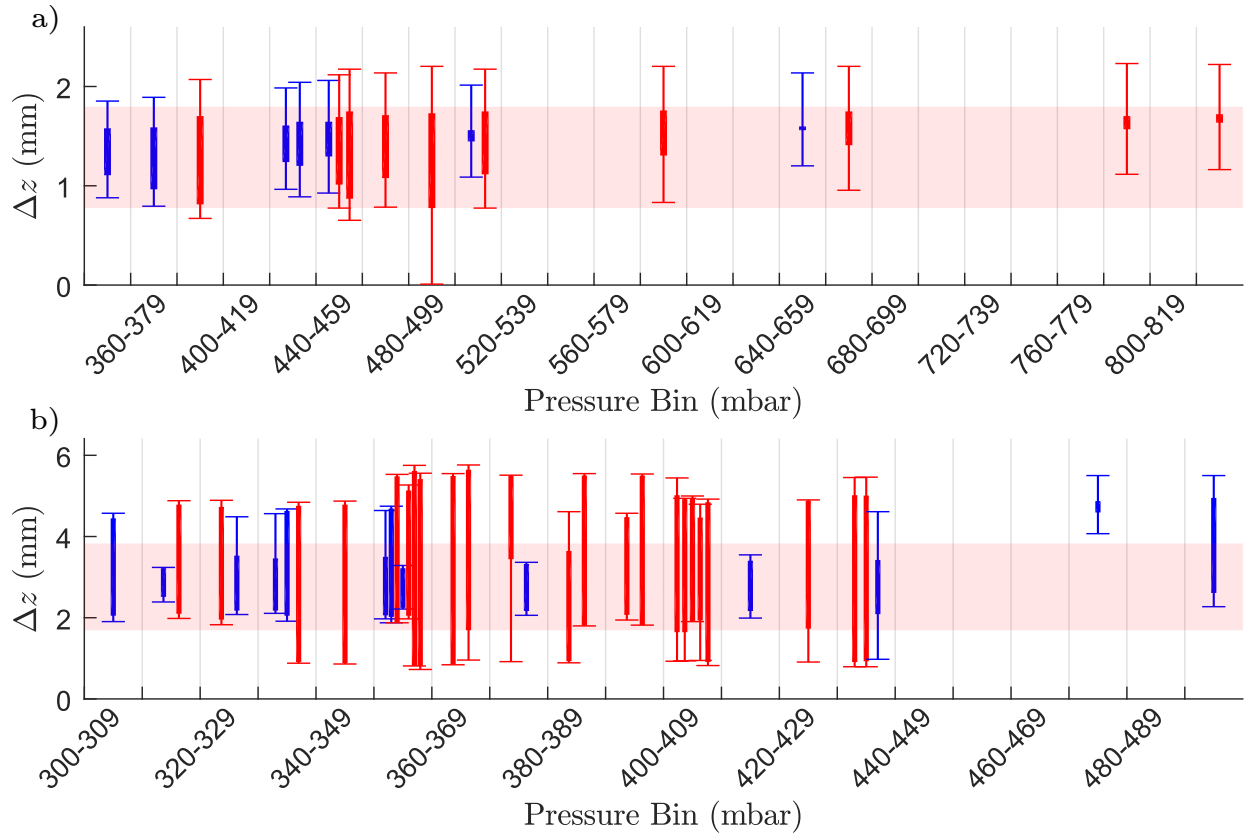
Figure 4. Example of aperture coverage in the axial direction (Δz) attained for a) trap type A and b) trap type B, using a He microplasma at $\Omega/2\pi = 23$ MHz. For ease of displaying multiple data points at identical pressures, the data is binned into consecutive pressure ranges (20 mbar in type A and 10 mbar in type B). For each data point, the error bars denote the plasma extremes and the boxed region indicates where the plasma symmetrically covers both sides of the aperture in the axial direction. The shaded region in each figure corresponds to the trapping zones of each device, which are the principal electrodes requiring surface processing. a) Trap type A aperture coverage data taken at $U_{RF} \leqslant 150$ V is in blue and $U_{RF} > 150$ V is in red. b) Trap type B aperture coverage data taken at $U_{RF} \leqslant 190$ V is in blue and $U_{RF} > 190$ V is in red.

get removed, there is little or no damage to the actual electrode surface. The energy threshold for sputtering of amorphous hydrocarbons by He, ϵ_{th}, can be calculated using the equation [57]

$$\epsilon_{th} = \left[7.0 \left(\frac{M_C}{M_{He}} \right)^{-0.54} + 0.15 \left(\frac{M_C}{M_{He}} \right)^{1.12} \right] \epsilon_{sb}, \quad (30)$$

where M_{He} and M_C are the masses of He and C atoms respectively, and $\epsilon_{sb} = 2.8$ eV is the surface binding energy for amorphous hydrocarbons [58]. From equation (30), ϵ_{th} was calculated to be 12.3 eV; figure 5d demonstrates that the microtrap devices operate in a regime where ϵ_{bom} is well below this threshold, and indeed substantially below the 57 eV threshold for He sputtering Au [23]. Consequently, the processing procedure for removal of adsorbed hydrocarbon contaminants will be reliant on the upper tail of the energy distribution.

The estimated sputtering time constants, $\tau_a = (\Phi_x \sigma_a)^{-1}$, for hydrocarbon surface adsorbates are presented in figure 6. Estimates for processing times t_{clean}, to achieve an arbitrary target adsorbate density N_t of 1 mm^{-2}, were calculated using equation (29) and a calculated value for σ_a. Up to 500 eV, σ_a is only weakly dependent on projectile energy, so we approximate it with the mean value in that range, $\sigma_a = 1.52 \times 10^{-20}$ m^2 [48, 49]. The auxiliary axis of figure 6 also shows the data scaled to t_{clean} for $N_t = 1$ mm^{-2}. The estimated surface processing times varied upwards from ~ 60 s over the P and U_{RF} ranges tested. Equation (29) shows that to reduce the adsorbate density by an extra factor of 100 requires an increase in t_{clean} of only $4.6\tau_a$. Figure 6 indicates that the flux of neutral atoms can have a substantial effect on the electrode surface that is comparable, if not greater, than the effect of the ions themselves. Other simulations and experiments have shown that fast neutrals can significantly contribute to the sputtering effect on the electrode surface [59–62]. For instance, in an O_2 plasma sputtering a Cr surface at $P = 0.01$ mbar, 30 % of the total rate of sputtering was attributed to
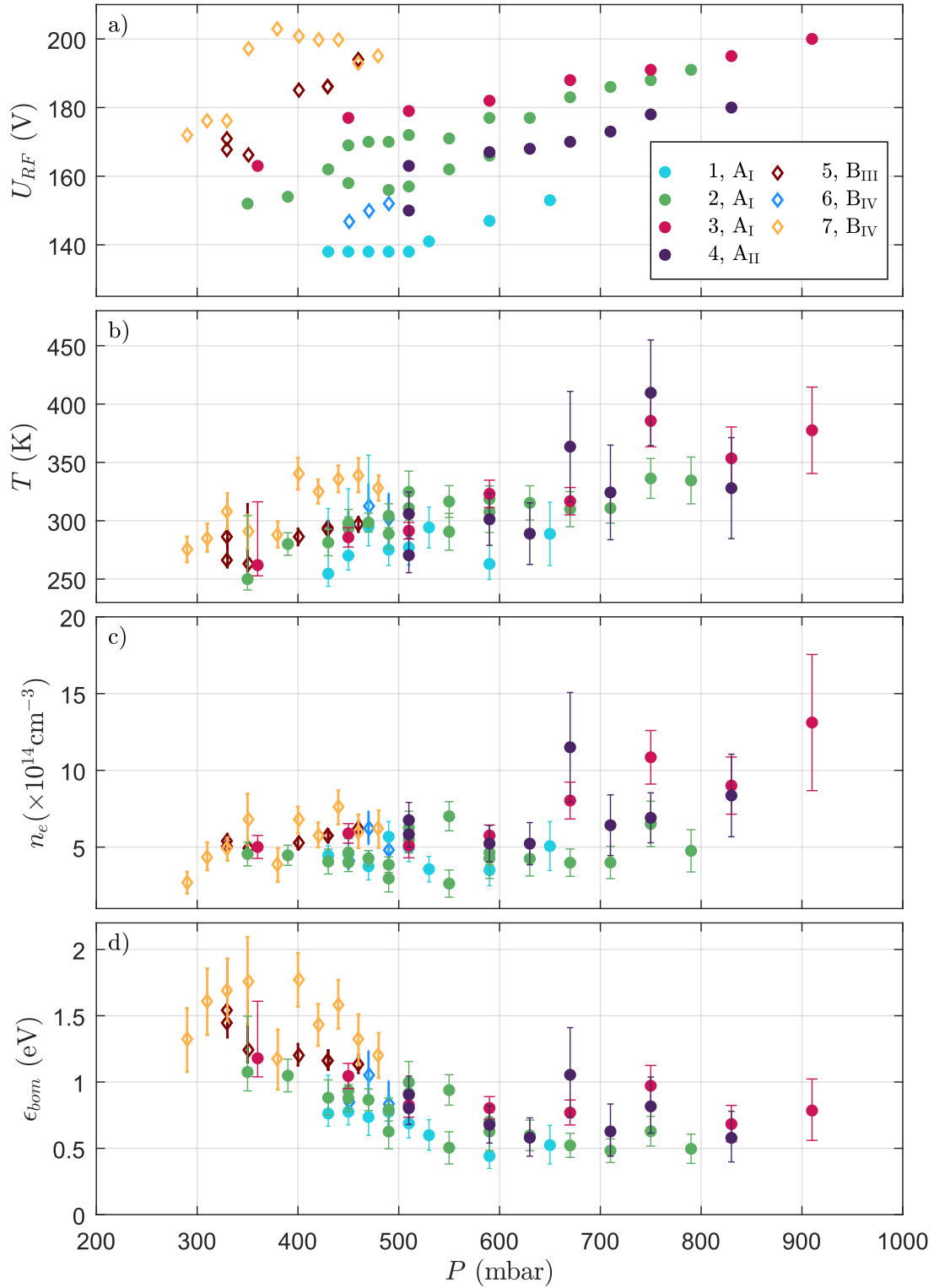
Figure 5. Measurements to determine the average ion bombardment energy with He at $\Omega_{RF}/2\pi = 23$ MHz. Four individual devices were used (denoted by subscripts I - IV in the legend). a) Operating U_{RF} values for a microplasma confined to the aperture with maximum coverage, for trials 1-4 in trap type A (circles) and trials 5-7 in trap type B (diamonds). b) T, and c) n_e, as measured from Voigt lineshapes fitted to the He I 667 nm and Hα 656 nm lines, using the U_{RF} from (a) and the method in section 2.3. d) ϵ_{bom} calculated from measured results in (a-c) via time-averaging of equation (22). The uncertainties in ϵ_{bom} values are propagated from those in T and n_e, which are described in the text. The legend shown in a) applies to all plots. Between trials with the same device, removal from vacuum and subsequent pre-trial preparation could contribute to the spread of pressure-voltage characteristics. Minor defects (e.g. surface quality and wirebonding) in devices of the same type will also contribute to differences in these characteristics.
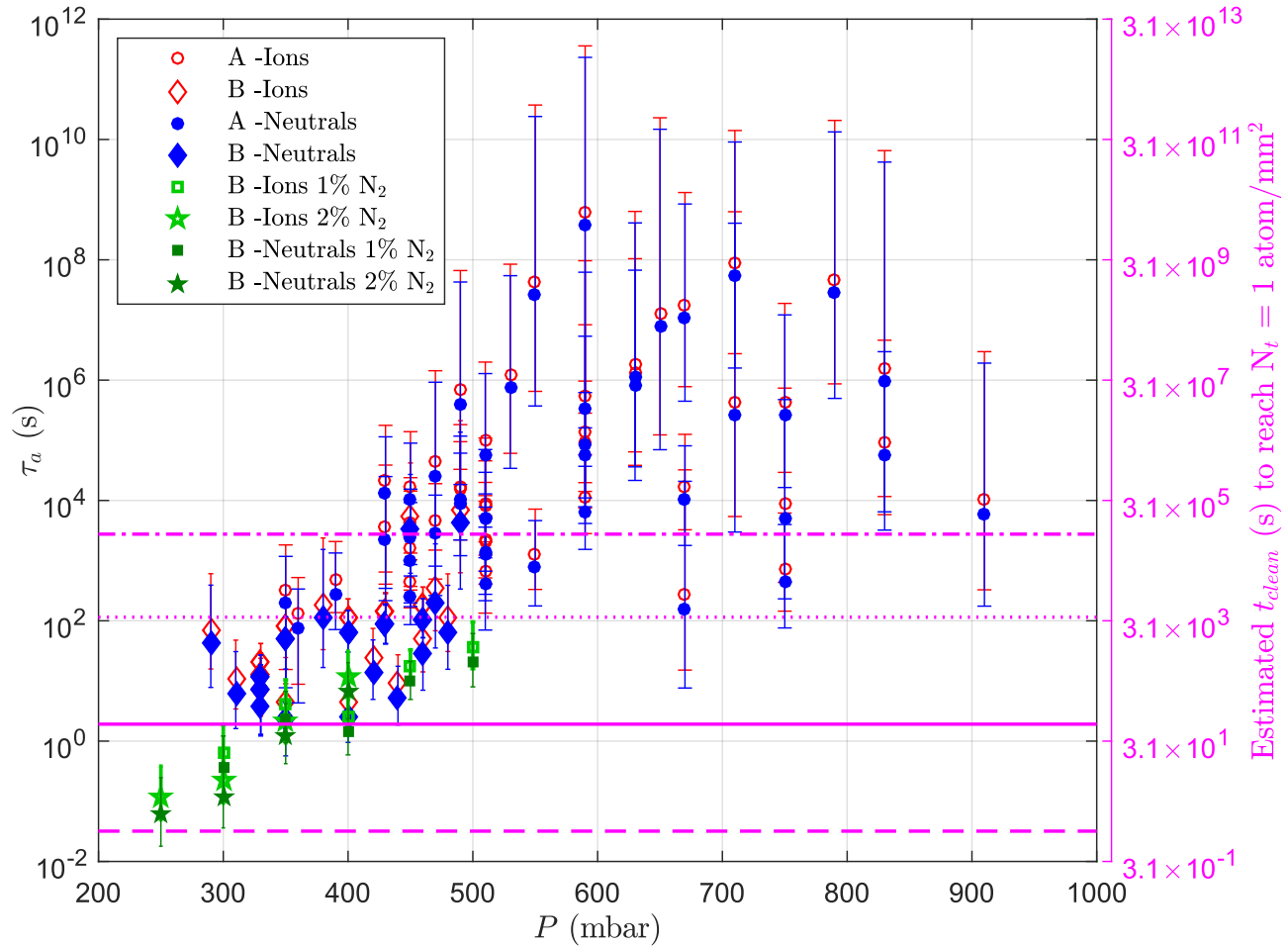
Figure 6. Estimated time constants τ_a for removal of hydrocarbon surface adsorbates on the microtrap electrodes. The estimates are based on fluxes calculated from measured plasma parameters. The τ_a due to ion flux are in open symbols, whereas those due to neutrals are in filled symbols. The latter are based on the mean of the upper and lower limits of the neutral flux. Error bars are propagated from the uncertainties in the spectroscopic measurements. The data is shown for He using trap types A and B (circles and diamonds respectively) and for trap type B using He with 1 % N_2 and 2 % N_2 (squares and stars respectively). The separated axis on the right of the graph shows the estimated time required to remove two monolayers of hydrocarbon adsorbates and reach a target adsorbate surface density of $N_t = 1$ atom/mm^2. The coloured horizontal lines indicate surface cleaning times of 1 s (dashed), 1 minute (solid), 1 hour (dotted) and 1 day (dashed and dotted).

neutrals [61]. As the pressure increases and the ion undergoes more collisions in the sheath, the relative proportion of fast neutrals generated is expected to increase.

For trap type B, since the microplasma approaches a homogeneous spread at higher voltages, the ions are more energetic and the estimated surface processing time is less than that for trap type A. For a microplasma that is well distributed in the aperture of trap type A, the optimal processing parameters are likely to be around $P = 360$ mbar and $U_{RF} = 160$ V for around 40 minutes. For trap type B, the optimum condition would be to operate the microplasma at $P = 350$ mbar and $U_{RF} = 200$ V, with $t_{clean} = 60$ s. However, it should be noted that the model presented here is merely an approximation, since it does not account for the exact nature of the transportation

of sputtered impurities. This same approximation was made in other work modelling microdischarges in coplanar geometries [60]. Sputtered contaminants could become negatively charged and confined within the plasma. Alternatively, after several collisions the sputtered particles can leave the plasma and diffuse in all directions to insignificant surfaces [51]. Finally, sputtered material may be redeposited on the electrode surfaces via back-diffusion or back-scattering processes [51]; in that case a greater t_{clean} would be required.

The effect of the microplasma on the electrode material itself can be estimated by considering the time constant for removal of gold surface layers, $\tau_{Au} = (\Phi_{He,max}\sigma_{He-Au})^{-1}$. Here, $\Phi_{He,max}$ is the maximum neutral He flux density in the range $\epsilon > \epsilon_{th} = 57$ eV (the Au sputtering threshold), and $\sigma_{He-Au} = 1.42 \times 10^{-20}$ m^2 is the calculated sputtering cross-section for

He with Au [48, 49]. In similar fashion to before, we calculate a weighted mean of $\sigma_{He+-He} = 1.2 \times 10^{-19}$ m^2 for energies greater than $\epsilon_{th} = 57$ eV. For the optimum processing parameters above, $\Phi_{He,max} \simeq 9.2 \times 10^4$ m^{-2}s^{-1} (trap type A) and $\Phi_{He,max} \simeq 7.1 \times 10^{10}$ m^{-2}s^{-1} (trap type B). Thus for the microplasmas observed in this work, we estimate $\tau_{Au,A} \simeq 7.8 \times 10^{14}$ s and $\tau_{Au,B} \simeq 1 \times 10^9$ s (where subscripts A and B denote the trap type), which are orders of magnitude greater than τ_a. These values of τ_{Au} show that sputtering of Au is expected to be negligible. To avoid electrical breakdown, it is important that Au is not sputtered and redeposited on the insulating SiO$_2$ surface (see figure 1a).

To verify that the electrodes were undamaged by the generation of the microplasma, images of internal Au surfaces in a type B ion trap were taken before and after an appropriate surface processing procedure (duration of 15 minutes, which for that particular data point was $\sim 27\tau_a$). Images were recorded at five axial (z) positions along the full extent of both an RF electrode, and also a DC electrode array. At each z position, three images were recorded along the x direction because the oblique viewing angle lacked sufficient depth of focus. In all positions but one, no difference was observed between the 'before' and 'after' images (see figure 7a,b). The end of the RF electrode was the one exception (see figure 7c,d) where a slight tarnishing near the corner tip was apparent. This effect is likely due to the localised high field emission which is a consequence of the electrode geometry. Since the effect is at a spatial location that is far removed from trapping zones it is considered to be negligible.

In addition to trials with pure He, gas mixtures of He and N$_2$ were tested. With N$_2$ it is possible to chemically sputter the hydrocarbon contaminants from the electrode surface, as opposed to the physical sputtering by He. The particular test devices used in this study were limited in applied U_{RF}, due to plasma formation around wirebond connections outside of the device aperture. Since N$_2$ has a higher breakdown voltage than He [63, 64], this limitation restricted the concentrations of N$_2$ in He to between 1 % and 2 %. The results for a single data set using a type B trap can be seen in figure 8. Further testing with the same trap has shown these results to be repeatable. The data for the He:N$_2$ mixtures shows the bounds of ϵ_{bom} in the range 1.2 eV $\leqslant \epsilon_{bom}$(He) $\leqslant$ 4.1 eV; these energies are approximately double those evident in the pure He microplasmas. From $P = 400$ - 500 mbar, the U_{RF} limit of the device under test was less than the amplitude required to achieve a microplasma extending across the full length of the device aperture. Figure 8e shows that, with this limitation, microplasma coverage of the trapping zones
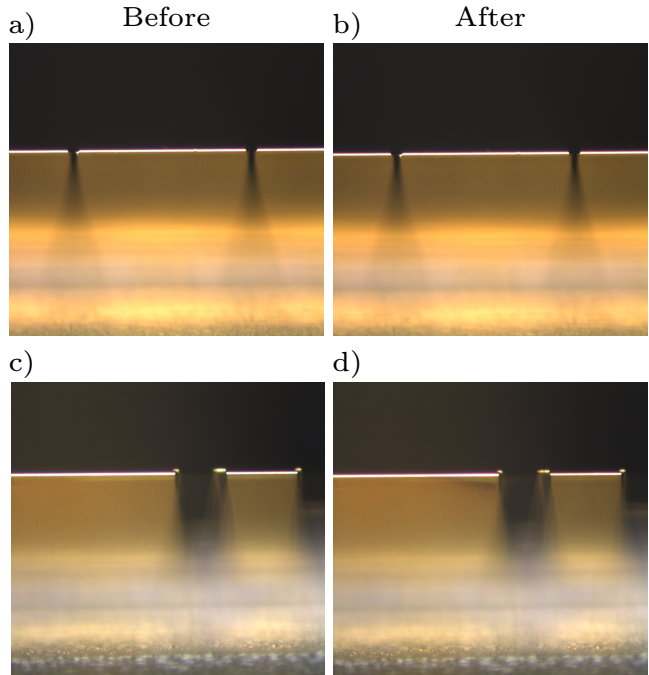

Figure 7. Sample pictures of electrode internal surfaces before and after microplasma processing with He at $P = 360$ mbar, $\Omega_{RF}/2\pi = 23$ MHz and $U_{RF} = 160$ V for 15 minutes ($\sim 27\tau_a$, where $\tau_a = 33$ s for these operating parameters). Centre of DC electrode array a) before and b) after microplasma processing. Similarly, one end of an RF electrode c) before and d) after processing. These images were recorded with the electrode's edge nearest the aperture in focus.

was almost complete at $P = \{350, 400\}$ mbar with 1 % N$_2$. To calculate ϵ_{bom} associated with the He ions the partial pressure of He:N$_2$ gas mixture was taken into account when calculating the sheath thickness s in equation (18). The estimated τ_a for the He:N$_2$ microplasmas are presented alongside the values for pure He microplasmas in figure 6. Similar to before, this also shows the estimated t_{clean} to achieve $N_t = 1$ mm^{-2}. This He:N$_2$ data shows lower τ_a than for pure He at the lowest pressures, which is due to achieving higher values of ϵ_{bom}. Estimated cleaning times are in the range 2 s $\leqslant t_{clean} \leqslant$ 650 s. These results suggest that a He:N$_2$ gas mixture could reduce surface processing times, in comparison to pure He. A more stringent comparison is to consider only the data where maximum coverage of the trapping zones was achieved. In that case, with 1 % N$_2$ in He at $P = 350$ mbar and 400 mbar, $t_{clean} = 74$ s and 43 s respectively. This is comparable to $t_{clean} = 60$ s at the optimum conditions for pure He as stated earlier.

5. Conclusions and outlook

We demonstrated a capacitively-coupled, RF microplasma inside the 3D electrode structure of an ion
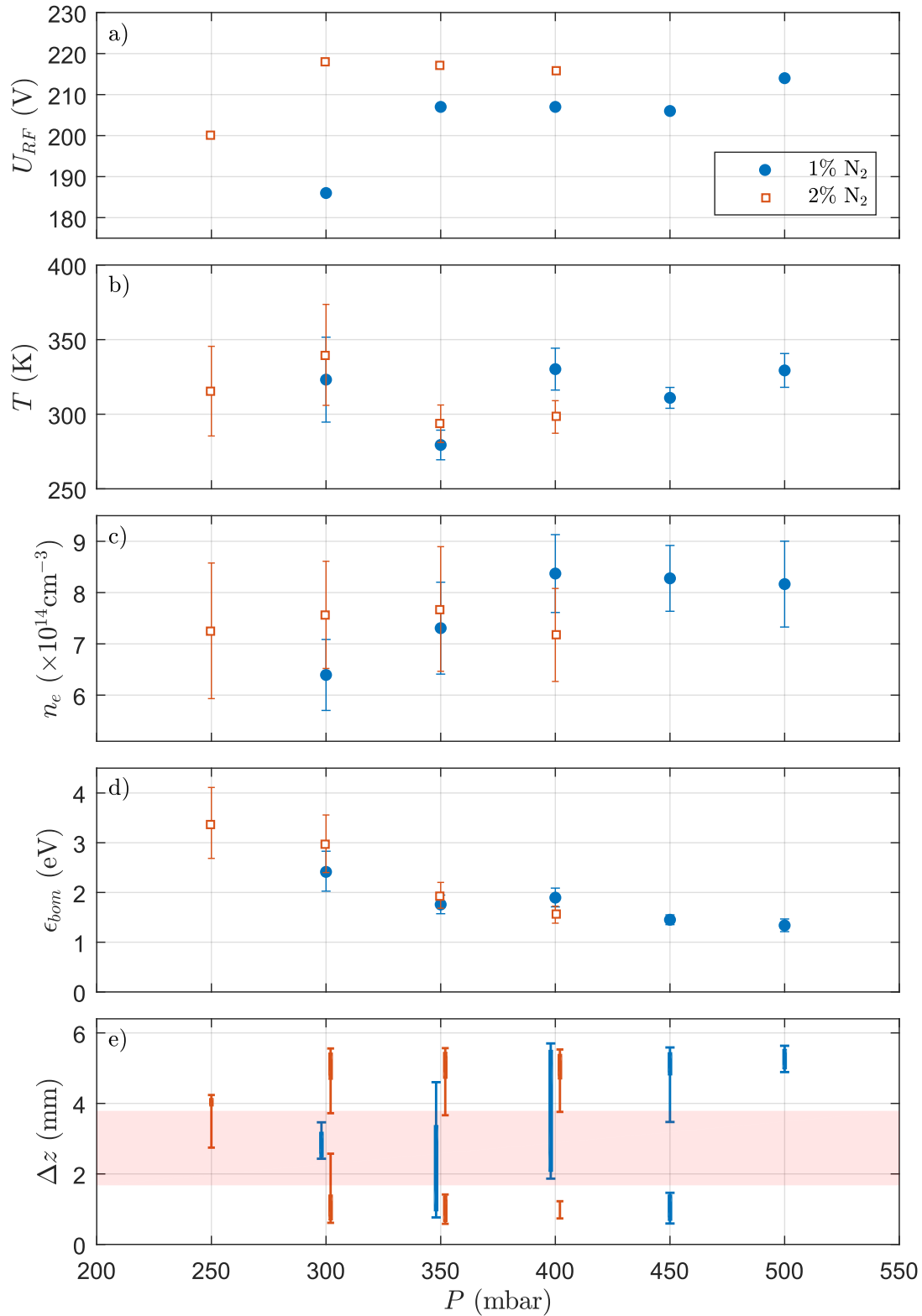
Figure 8. Measurements to determine the average ion bombardment energy with a He:N$_2$ mixture at $\Omega_{RF}/2\pi = 23$ MHz. a) Operating U_{RF} values for a microplasma confined to the aperture of trap type B, for N$_2$ concentrations of 1 % (filled circles) and 2 % (empty squares). b) T, and c) n_e, as measured from Voigt lineshapes fitted to the He I 667 nm and Hα 656 nm lines, using the U_{RF} from (a) and the method in section 2.3. d) ϵ_{bom} calculated from measured results in (a-c) via time-averaging of equation (20). The uncertainties in ϵ_{bom} are propagated due to those in T and n_e, determined in a similar manner to that for the pure He data. The axial spatial extent Δz of the microplasmas in this data set is shown in e); at $P = \{300, 350, 400\}$ mbar the range bars are offset slightly from the exact P for clarity.

microtrap device. The parameters associated with a He microplasma, *i.e.* gas temperature T and electron density n_e, were both determined by OES of the He I 667 nm and Hα 656 nm lines, without perturbing the microplasma. Mean ion bombardment energies were calculated using the measured T and n_e. Our results suggest that the microplasma technique is suited to *in situ* selective removal of surface adsorbates from ion microtrap electrodes.

Due to the highly collisional nature of the microplasma, the mean ion energies were found to be much lower than the sputtering thresholds of both the hydrocarbons and Au. It was found that in a He microplasma, 0.3 eV $\leqslant \epsilon_{bom}$(He) $\leqslant$ 2.1 eV. Testing with a He:N$_2$ gas mixture indicated that higher ion energies in the range 1.2 eV $\leqslant \epsilon_{bom}$(He) $\leqslant$ 4.1 eV can be achieved. Concerning the suitability of these microplasmas as a technique for the selective removal of surface adsorbates from ion microtrap electrodes, it will be reliant on the high energy tail of the energy distribution. Estimated surface processing times were calculated and showed that cleaning times down to $\sim$ 40 minutes for type A microtrap chips should be sufficient for removal of two hydrocarbon monolayers. For trap type B, corresponding times were estimated to be 60 s. Under operating parameters for these results, the microplasma extent across all trapping zone electrodes was almost complete for type A and complete for type B. For He:N$_2$ mixtures under the same electrode coverage condition, the estimated cleaning time was in the range 43 s $\leqslant t_{clean} \leqslant$ 74 s. During these times, the sputtering of Au from the electrode surface is expected to be negligible, which was confirmed by optical microscopy.

The principle of the microplasma technique presented here is widely applicable to other ion traps with a 3D electrode geometry, both micro-structured and otherwise. Furthermore, it is possible that the general principle could also be applied to microtraps with a 2D electrode geometry. In principle, the technique should be applicable to a range of metallic electrode materials.

For effective use as an ion microtrap, the device must be contained in vacuum at around 10^{-11} mbar. Earlier work has shown that hydrocarbons adsorb onto electrode surfaces during vacuum bakeout to reach this pressure [17]. Therefore, it is necessary to conduct the proposed microplasma surface treatment process after this bakeout, while recovering to a similarly low pressure after post-processing pump down. This will require the microplasma gas to be of the highest purity grade and be introduced via vacuum-baked gas lines, such that residual gas analysis of the evacuated chamber shows recovery of the pre-processing condition. Furthermore, it is necessary that

any gas used does not react with elemental species in the vacuum. The use of an inert gas such as He is advantageous for such a procedure. While the aforementioned procedure is possible in principle, care will be required in order to achieve the desired cleanliness for $\sim 10^{-11}$ mbar pressure upon post-processing pump down.

When operating the microplasma after the system bakeout to achieve $\sim 10^{-11}$ mbar, water vapour will be virtually eliminated from the vacuum chamber. Therefore, the Hα 656 nm line needed for the OES will be absent, but this is not a significant problem. The analysis presented here shows that a suitable combination of P(He), $\Omega_{RF}/2\pi$ and U_{RF} can be predetermined, so that n_e and T are well defined and the resultant ϵ_{bom} and t_{clean} is known. Thus, it seems reasonable to conclude that with careful measurements characterising the procedure on an identical system, spectroscopic measurements during the actual microplasma processing step after bakeout are not necessary.

The current study shows that there is experimental evidence to suggest that a small fraction of ions and neutrals in the microplasma are sufficiently energetic to remove amorphous hydrocarbon adsorbates. In principle, it is possible to record the temporal evolution of the sputtering process via optical emission from the sputtered film, e.g. via CH(A-X) spectral line at 431 nm [65]. However, our apparatus does not have the sensitivity to detect such emission due to the much thinner surface adsorbate film expected on our devices [66]. Further experimental work with a more complex apparatus could be done to investigate this, where the ion microtrap and microplasma system are incorporated with a surface analysis apparatus. This would permit analysis of a contaminated surface immediately before and after *in situ* microplasma processing without exposure to atmosphere, similar to the approach of [17]. However, the true effectiveness of the microplasma technique for its intended purpose will only become apparent with a direct comparison of trapped-ion heating rates measured before and after processing.

Previous work using energetic ion beams removed not only the hydrocarbon contamination, but also the electrode material [17, 18, 25]. The method that we describe here operates at much lower bombardment energies, and so offers the prospect for selective removal of only the surface adsorbates. The technique could be particularly useful in future studies of electric field noise, for separating the effects of surface cleanliness from any due to electrode surface order [25].

Acknowledgements

Funding

Appendix A. Calculation of plasma parameters

The calculations of the average particle bombardment energy, the particle flux and the cleaning time all rely on the knowledge of three plasma parameters, which themselves are dependent on the electron density n_e and the gas temperature T (i.e. those parameters measured by spectroscopy). The first of these parameters is the electron temperature $T_e(T)$ in the bulk of the microplasma; along with n_e, this enables the ion velocity $u_s(n_e, T)$ and ion density $n_s(n_e, T)$ at the sheath edge to be calculated. This appendix describes the analysis for determining the values of $T_e(T)$, $u_s(n_e, T)$ and $n_s(n_e, T)$. Unless stated otherwise, all equations in this appendix are from [28] (with appropriate modifications to incorporate all parameters in SI units). The assumed operating regime is that of a low-frequency, capacitively-coupled discharge at high pressure and with high-voltage, collisional sheaths.

Appendix A.1. Electron Temperature in a High Pressure Discharge

In the bulk of the microplasma at high pressures, T_e can be found by numerically solving the equation

$$\frac{\left[K_{mi}(T)K_{iz}(T_e)\right]^{1/2}}{u_B(T_e)} = \frac{\pi}{n_g(T)l}, \qquad (A.1)$$

where K_{mi} and n_g are functions of T, and K_{iz} and u_B are functions of T_e. Here K_{mi} is the rate constant for ion-neutral collisions in which momentum transfer occurs. K_{iz} is the ionisation rate constant, u_B is the Bohm velocity, n_g is the gas density and l is the electrode separation. The Bohm velocity is defined by

$$u_B = \left(\frac{k_B T_e}{M}\right)^{1/2} \qquad (A.2)$$

where M denotes the ion mass.

The ion velocity in the microplasma bulk, u_0, is required to calculate K_{mi}:

$$K_{mi} = u_0 \sigma_{He^+ - He, B}. \qquad (A.3)$$

where $\sigma_{He^+ - He, B} = 5 \times 10^{-19}$ m^2 is the calculated He ion and neutral atom collisional cross-section in the plasma bulk [28, 67]. Due to the highly collisional nature of the discharge, the ions in the microplasma bulk are assumed to be in thermal equilibrium with the neutral atoms. Therefore, assuming a Maxwellian distribution associated with the ions,

$$u_0 = \left(\frac{8k_B T}{\pi M}\right)^{1/2} \qquad (A.4)$$

and so equation (A.3) can be rewritten as

$$K_{mi} = \sigma_{He^+ - He}\left(\frac{8k_B T}{\pi M}\right)^{1/2}. \qquad (A.5)$$

In contrast, the atom ionisation rate constant K_{iz} requires knowledge of the electron velocity in the bulk of the microplasma, u_e. Similar to above, this is determined by assuming a Maxwellian distribution of electron energies, thus

$$u_e = \left(\frac{8k_B T_e}{\pi m}\right)^{1/2}, \qquad (A.6)$$

where m is the mass of the electron. Strictly speaking, the microplasma generated should have an electron energy distribution (EED) that consists of three groups [27, 53]; a) the low energy electrons that are confined by the ambipolar potential in the microplasma bulk, b) the mid-energy electrons capable of escaping from the discharge, and c) the high-energy electrons due to accelerated secondary electrons in the sheath. Here, the high-energy tail of the distribution within the microplasma bulk can be neglected due to the short penetration depth when compared to the inter-electrode distance [27]. The EED is therefore more accurately described by a bi-Maxwellian distribution. However, it should be noted that the density of the mid-energy electrons is several orders of magnitude smaller than that of the low energy electrons. We find that the error associated with the average electron energy, due to neglecting the mid-energy electrons, is small in comparison to the statistical error in fitting the spectral lines.

Using equation (A.6), K_{iz} can be calculated as

$$K_{iz} = \sigma_0 u_e \left(1 + \frac{2k_B T_e}{\epsilon_{iz}}\right) \exp\left(\frac{-\epsilon_{iz}}{k_B T_e}\right). \qquad (A.7)$$

Here ϵ_{iz} is the atom ionisation energy and σ_0 is a constant associated with the ionisation cross-sectional area

$$\sigma_0 = \pi \left(\frac{e}{4\pi\epsilon_0\epsilon_{iz}} \right)^2, \qquad (A.8)$$

where ϵ_0 is the permittivity of free space. For a He discharge $\epsilon_{iz} = 24.6$ eV.

Equations (A.2), (A.5) and (A.7) are substituted into equation (A.1), along with $n_g(T)$ and l. The resulting equation is solved numerically using a Newton-Raphson algorithm to find T_e.

Appendix A.2. Ion Density at the Sheath Edge

For a high pressure discharge, the ion density at the sheath edge n_s can be found using u_0 and K_{mi} from equations (A.4) and (A.5) respectively, in conjunction with the ambipolar diffusion coefficient D_a. At high pressures, D_a is

$$D_a = \frac{k_B T_e}{M n_g K_{mi}}. \qquad (A.9)$$

The quantities u_0, K_{mi}, D_a and l can then be substituted into the equation

$$\frac{n_s}{n_0} = \left[1 + \left(\frac{l u_B}{\pi D_a} \right)^2 \right]^{-1/2}, \qquad (A.10)$$

where n_0 is the ion density in the bulk of the microplasma. The quasi-neutrality condition in the bulk region of the microplasma entails that $n_0 \simeq n_e$. Thus equation (A.10) can be rewritten as

$$n_s(n_e, T) \simeq n_e \left[1 + \left(\frac{l u_B(T)}{\pi D_a(T)} \right)^2 \right]^{-1/2}, \qquad (A.11)$$

where the n_e and T functional dependencies are indicated in parentheses.

Appendix A.3. Ion Velocity at Sheath Edge

The ion velocity at a collisional sheath edge, u_s, is calculated using

$$u_s(n_e, T) = \frac{u_B(T)}{\left(1 + \frac{\pi \lambda_{Ds}(n_e, T)}{2\lambda_i(T)} \right)^{1/2}}, \qquad (A.12)$$

where the n_e and T dependencies are indicated in parentheses. Equations (A.2) and (17) give u_B and the mean free path λ_i respectively. The Debye length at sheath edge (in m) is given by λ_{Ds}

$$\lambda_{Ds} = \left(\frac{\epsilon_0 k_B T_e}{e^2 n_s} \right)^{1/2}, \qquad (A.13)$$

where T_e and n_s are calculated using the methods in the previous two sections.

References

[1] Ladd T D, Jelezko F, Laflamme R, Nakamura Y, Monroe C and O'Brien J L 2010 *Nature* **464** 45–53

[2] Friedenauer A, Schmitz H, Glueckert J T, Porras D and Schätz T 2008 *Nat. Phys.* **4** 757–761

[3] Giovannetti V, Lloyd S and Maccone L 2011 *Nat. Photonics* **5** 222–229

[4] Chou C W, Hume D B, Koelemeij J C J, Wineland D J and Rosenband T 2010 *Phys. Rev. Lett.* **104** 070802

[5] Blatt R and Wineland D 2008 *Nature* **453** 1008–1015

[6] Safavi-Naini A, Rabl P, Weck P F and Sadeghpour H R 2011 *Phys. Rev. A* **84** 023412

[7] Hughes M D, Lekitsch B, Broersma J A and Hensinger W K 2011 *Contemp. Phys.* **52** 505–529

[8] Turchette Q A, Kielpinski, King B E, Leibfried D, Meekhof D M, Myatt C J, Rowe M A, Sackett C A, Wood C S, Itano W M, Monroe C and Wineland D J 2000 *Phys. Rev. A* **61** 063418

[9] Deslauriers L, Olmschenk S, Stick D, Hensinger W K, Sterk J and Monroe C 2006 *Phys. Rev. Lett.* **97** 103001

[10] Kumph M, Henkel C, Rabl P, Brownnutt M and Blatt R 2016 *New J. Phys.* **18** 23020

[11] Boldin I A, Kraft A and Wunderlich C 2018 *Phys. Rev. Lett.* **120** 23201

[12] Sedlacek J A, Greene A, Stuart J, McConnell R, Bruzewicz C D, Sage J M and Chiaverini J 2018 *Phys. Rev. A* **97** 020302

[13] Wineland D, Monroe C, Itano W, Leibfried D, King B and Meekhof D 1998 *J. Res. Natl. Inst. Stand. Technol.* **103** 259

[14] Labaziewicz J, Ge Y, Antohi P, Leibrandt D, Brown K R and Chuang I L 2008 *Phys. Rev. Lett.* **100** 013001

[15] Chiaverini J and Sage J M 2014 *Phys. Rev. A* **89** 012318

[16] Bruzewicz C D, Sage J M and Chiaverini J 2015 *Phys. Rev. A* **91** 041402

[17] Hite D A, Colombe Y, Wilson A C, Brown K R, Warring U, Jördens R, Jost J D, McKay K S, Pappas D P, Leibfried D and Wineland D J 2012 *Phys. Rev. Lett.* **109** 103001

[18] Daniilidis N, Gerber S, Bolloten G, Ramm M, Ransford A, Ulin-Avila E, Talukdar I and Häffner H 2014 *Phys. Rev. B* **89** 245435

[19] Kim E, Safavi-Naini A, Hite D A, McKay K S, Pappas D P, Weck P F and Sadeghpour H R 2017 *Phys. Rev. A* **95** 033407

[20] Wilpers G, See P, Gill P and Sinclair A G 2012 *Nat. Nanotechnol.* **7** 572–576

[21] See P, Wilpers G, Gill P and Sinclair A G 2013 *J. Microelectromechanical Syst.* **22** 1180–1189

[22] Wilpers G, See P, Gill P and Sinclair A G 2013 *Appl. Phys. B Lasers Opt.* **111** 21–28

[23] Behrisch R and Eckstein W 2007 *Sputtering by Particle Bombardment* (Springer)

[24] McConnell R, Bruzewicz C, Chiaverini J and Sage J 2015 *Phys. Rev. A* **92** 020302

[25] Hite D A, McKay K S, Kotler S, Leibfried D, Wineland D J and Pappas D P 2017 *MRS Adv.* **2** 2189–2197

[26] Belostotskiy S G, Ouk T, Donnelly V M, Economou D J and Sadeghi N 2010 *J. Appl. Phys.* **107** 053305

[27] Iza F, Kim G J, Lee S M, Lee J K, Walsh J L, Zhang Y T and Kong M G 2008 *Plasma Process. Ploymers* **5** 322–344

[28] Lieberman M A and Lichtenberg A J 2005 *Principles of Plasma Discharges and Materials Processing* 2nd

ed (Wiley-Interscience)

[29] Balcon N, Aanesland a and Boswell R 2007 *Plasma Sources Sci. Technol.* **16** 217–225

[30] Zhu X M, Walsh J L, Chen W C and Pu Y K 2012 *J. Phys. D. Appl. Phys.* **45** 295201

[31] Sismanoglu B, Cunha C, Gomes M, Caetano R and Grigorov K 2010 *Brazilian J. Phys.* **40** 459–463

[32] Hofmann S, van Gessel A F H, Verreycken T and Bruggeman P 2011 *Plasma Sources Sci. Technol.* **20** 065010

[33] Horvatic V, Veza D, Vadla C and Franzke J 2014 *J. Anal. At. Spectrom.* **29** 498–505

[34] Djurović S F o S and Konjević N F o P 2009 *Plasma Sources Sci. Technol.* **18** 035011

[35] Griem H 1964 *Plasma Spectroscopy* (McGraw-Hill Book Company)

[36] Gigosos M A and Cardeñoso V 1996 *J. Phys. B At. Mol. Opt. Phys.* **29** 4795–4838

[37] Akermark T, Hultquist G and Lu Q 1996 *J. Mater. Eng. Perform.* **5** 516–520

[38] Fridman A 2008 *Plasma Chemistry* (Cambridge University Press)

[39] Konjevic R and Konjevic N 1997 *Spectrochim. Acta Part B* **52** 2077–2084

[40] Park H S, Kim S J, Joh H M, Chung T H, Bae S H and Leem S H 2010 *Phys. Plasmas* **17** 033502

[41] Drake G W F 2006 *Springer Handbook of Atomic, Molecular, and Optical Physics* 1st ed (New York, NY: Springer-Verlag New York)

[42] Namba S, Yamasaki T, Hane Y, Fukuhara D, Kozue K and Takiyama K 2011 *J. Appl. Phys.* **110** 073307

[43] Griem H R 1974 *Spectral Line Broadening by Plasmas* vol 39 (Academic Press inc.)

[44] Griem H R, Baranger M, Kolb A C and Oertel G 1962 *Phys. Rev.* **125** 177–195

[45] NIST Atomic Spectra Database

[46] Hagelaar G J M, Kroesen G M W and Klein M H 2000 *J. Appl. Phys.* **88** 2240–2245

[47] Mahadevan P and Magnuson G D 1968 *Phys. Rev.* **171** 103–109

[48] Taglauer E 1990 *Appl. Phys. A Solids Surfaces* **51** 238–251

[49] Winters H F and Sigmund P 1974 *J. Appl. Phys.* **45** 4760–4766

[50] Winchester M R and Payling R 2004 *Spectrochim. Acta - Part B At. Spectrosc.* **59** 607–666

[51] Ferreira N P and Büger P A 1978 *Zeitschrift für Naturforsch. A* **33** 16–19

[52] Kotz J, Treichel P and Weaver G 2006 *Chemistry and Chemical Reactivity, Enhanced Review Edition* (Thomson Books/Cole)

[53] Lin L and Wang Q 2015 *Plasma Chem. Plasma Process.* **35** 925–962

[54] Wang Q, Koleva I, Donnelly V M and Economou D J 2005 *J. Phys. D. Appl. Phys.* **38** 1690–1697

[55] Konjević N 1999 *Phys. Rep.* **316** 339–401

[56] Moravej M, Yang X, Nowling G R, Chang J P, Hicks R F and Babayan S E 2004 *J. Appl. Phys.* **96** 7011–7017

[57] García-Rosales C, Eckstein W and Roth J 1995 *J. Nucl. Mater.* **218** 8–17

[58] Jacob W, Hopf C and Schlüter M 2006 *Phys. Scr.* **T124** 32–36

[59] Ito T and Cappelli M A 2007 Energetic neutral particle production in the cathode sheath of direct-current discharges *ISPC-18* (Kyoto, Japan) pp 4–7

[60] Pitchford L C, Wang J, Piscitelli D and Boeuf J P 2006 *IEEE Trans. Plasma Sci.* **34** 351–359

[61] Hsieh J H and Li C 2003 *Jpn. J. Appl. Phys.* **42** 5295–5298

[62] Mason R and Pichilingi M 1994 *J. Phys. D. Appl. Phys.* **27** 2363

[63] Brandenburg, R; Wagner, H, Michel, P, Trunec, D, Stahel P 2003 Diffuse dielectric barrier discharges in nitrogen-containing gas mixtures *Int. Conf. Phenom. Ioniz. Gases [26th] Vol. 4* (Greifswald,)

[64] Tschiersch R, Bogaczyk M and Wagner H E 2014 *J. Phys. D. Appl. Phys.* **47** 365204

[65] Hansen T A R, Colsters P G J, Weber J W, van de Sanden M C M and Engeln R 2009 Amorphous hydrogenated carbon etching with a plasma jet *ISPC-19* pp 2–5

[66] Mangolini F, McClimon J B, Rose F and Carpick R W 2014 *Anal. Chem.* **86** 12258–12265

[67] Rapp D and Francis W E 1962 *J. Chem. Phys.* **37** 2631–2645